arXiv:1612.04356v1 [cond-mat.mtrl-sci] 13 Dec 2016

Multiple structural transitions driven by spin-phonon couplings in a perovskite oxide

Claudio Cazorla,[1,*] Oswaldo Diéguez,[2] and Jorge Íñiguez[3]

[1] *School of Materials Science and Engineering, UNSW Australia, Sydney NSW 2052, Australia*
Integrated Materials Design Centre, UNSW Australia, Sydney NSW 2052, Australia
[2] *Department of Materials Science and Engineering,*
Faculty of Engineering, Tel Aviv University, IL-69978 Tel Aviv, Israel
The Raymond and Beverly Sackler Center for Computational Molecular
and Materials Science, Tel Aviv University, IL-69978 Tel Aviv, Israel
[3] *Materials Research and Technology Department,*
Luxembourg Institute of Science and Technology (LIST),
5 avenue des Hauts-Fourneaux, L-4362 Esch/Alzette, Luxembourg

Spin-phonon interactions are central to many interesting phenomena, ranging from superconductivity to magnetoelectric effects. Yet, they are believed to have a negligible influence on the structural behavior of most materials. For example, magnetic perovskite oxides often undergo structural transitions accompanied by magnetic signatures whose minuteness suggests that the underlying spin-phonon couplings are largely irrelevant. Here we present an exception to this rule, showing that novel effects can occur as a consequence. Our first-principles calculations reveal that spin-phonon interactions are essential to reproduce the experimental observations on the phase diagram of magnetoelectric multiferroic $BiCoO_3$. Moreover, we predict that, under compression, these couplings lead to an unprecedented temperature-driven double-reentrant sequence of ferroelectric transitions. We propose how to modify $BiCoO_3$ via chemical doping to reproduce such striking effects at ambient conditions, thereby yielding useful multifunctionality.

Most ferroelectric (FE) and ferroelastic perovskite oxides undergo transitions involving structurally similar phases. One might guess that spin-phonon (SP) effects should play a role in such transformations, as it occurs in materials exhibiting more drastic changes (e.g., Ni-based superalloys or steal) [1, 2]. Yet, excepting the especial case of compounds in which a magnetically-driven symmetry breaking yields ferroelectric order [3], SP couplings tend to have no impact. Even in compounds like room-temperature multiferroic $BiFeO_3$ (BFO), in which SP effects affect significantly the free energy of competing phases, their influence on the structural transitions is minor [4].

Figure 1 shows the relevant polymorphs in BFO. The rhombohedral FE phase ($\mathcal{R}$) that is stable at ambient conditions displays displacements of the Bi cations and concerted antiphase rotations of the O_6 octahedra about the polar [111] axis. (Axes are given in the pseudo-cubic setting.) There is also a paraelectric (PE) phase characterized by antiphase O_6 tilts about [110] and in-phase rotations about [001]. This orthorhombic ($\mathcal{O}$) structure is stable above 1100 K [6]. Magnetism in these phases is dominated by a strong antiferromagnetic (AFM) superexchange between adjacent irons, and first-principles-derived spin models yield a Néel temperature of about 600 K for both of them [4]. Further, SP couplings turn out to be very similar in both structures and thereby have a minute impact on their relative stability [4].

We can conjecture that, for SP couplings to have a strong influence on the structural transitions, the magnetic interactions in the competing polymorphs need to be as different as possible. Interestingly, perovskite $BiCoO_3$ (BCO) – also a room-temperature multiferroic – complies with this requirement [7]. At ambient conditions BCO presents a FE tetragonal ($\mathcal{T}$) phase with polarization along [001] (Fig. 1c) and a very distorted cell with aspect ratio approaching 1.3. Consequently, the magnetic interactions within a plane are stronger than across planes, rendering a relatively low Néel temperature of about 310 K, according to our first-principles estimate. (See Supplementary Information for more on this result and its comparison to experiment.) At high temperatures, BCO presents a PE $\mathcal{O}$ phase with $c/a \approx 1$ and a three-dimensional spin lattice; our corresponding first-principles-based Heisenberg model yields $T_N \approx 500$ K. As the spin-spin interactions, we expect the SP couplings in BCO's $\mathcal{T}$ and $\mathcal{O}$ phases to also differ significantly.

SP-controlled transitions at ambient pressure

To test this, we compute the free energy of BCO's $\mathcal{T}$ and $\mathcal{O}$ phases as a function of temperature, following the first-principles approach of Ref. [4] (see Methods). We obtain a critical temperature at zero pressure of $T_c^{\rm the}(0) = 890(50)$ K, in agreement with the experimental value $T_c^{\rm exp}(0) = 850(75)$ K [8] [Fig. 2(a)]. Note that the $\mathcal{T}$–$\mathcal{O}$ transition occurs at a temperature at which both phases are paramagnetic (PM), and that our method accounts for the contribution of disordered spins to the free energy. Interestingly, if the spins are frozen in their ground-state configuration, the transition is predicted to occur at 2350(50) K, which is unrealistically high [Fig. 2(b)]. Hence, we find that magnetic disorder greatly contributes to the stabilization of the $\mathcal{O}$ phase, and that SP effects are critical to reproduce the

* Corresponding Author

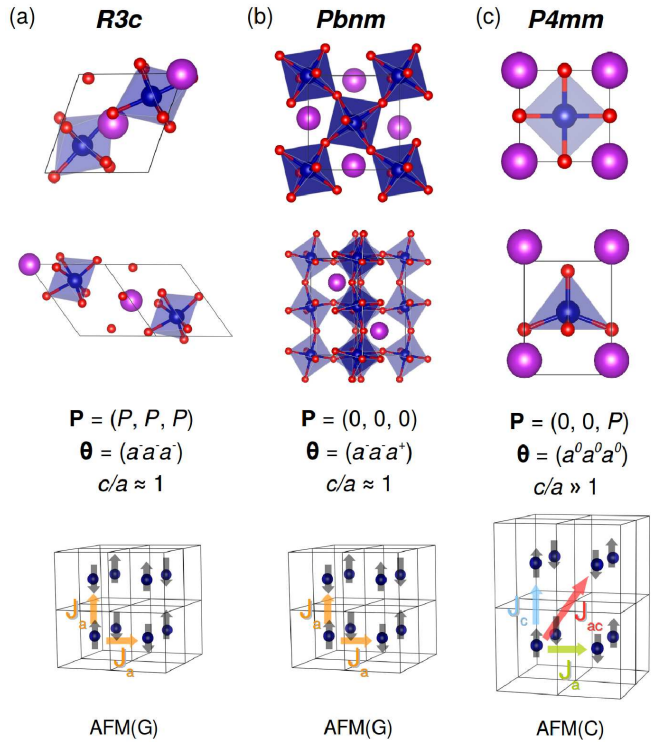

FIG. 1. Structural and magnetic properties of energetically competitive polymorphs in bulk $BiFeO_3$ and $BiCoO_3$: (a) rhombohedral $R3c$ ($\mathcal{R}$), (b) orthorhombic $Pbnm$ ($\mathcal{O}$), and (c) tetragonal $P4mm$ ($\mathcal{T}$). Patterns of O_6 octahedra rotations are expressed in Glazer's notation [5]. The c/a aspect ratio of pseudo-cubic lattice parameters is approximately 1 for the $\mathcal{R}$ and $\mathcal{O}$ phases, while it is about 1.3 for the so-called *super-tetragonal* $\mathcal{T}$ structure. Sketches of the lowest-energy spin configurations and exchange constants for a Heisenberg spin model of each phase are also shown.

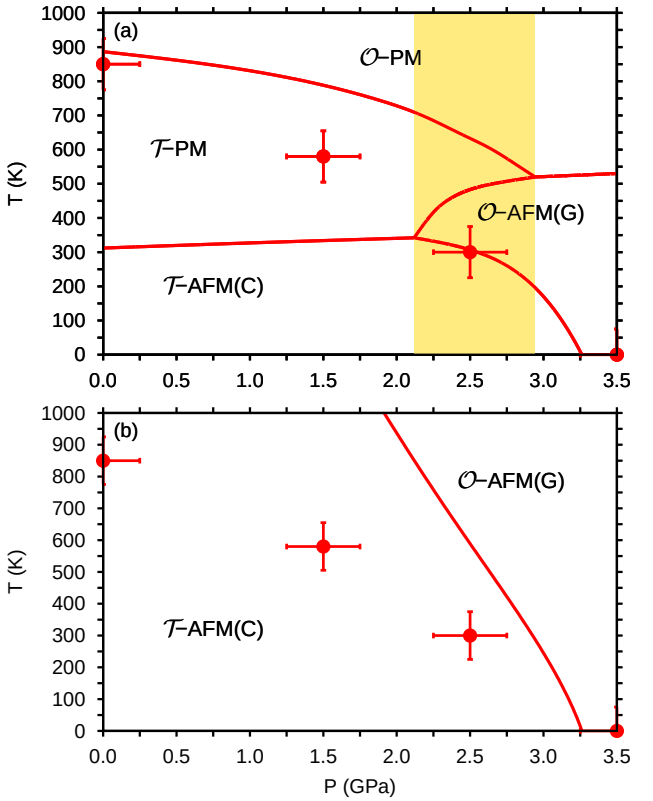

FIG. 2. $P-T$ phase diagram of bulk $BiCoO_3$ calculated from first principles. (a) Spin-phonon coupling effects are considered in the calculation of quasi-harmonic free energies. Multiple T-induced multiferroic phase transitions occur in the region colored in yellow. (b) Fixed magnetic spin order (corresponding to the lowest-energy spin arrangement) is imposed in the calculation of quasi-harmonic free energies. Experimental data corresponding to the ferroelectric to paraelectric phase transition [8] are shown for comparison (solid dots).

experimental T_c.

To understand this, note how the Γ-phonon frequencies change when considering AFM and FM (ferromagnetic) spin orders in the $\mathcal{T}$ and $\mathcal{O}$ phases. These frequency shifts, $\Delta\omega \equiv \omega_{\rm AFM} - \omega_{\rm FM}$, reflect the magnitude of SP couplings [9] and their sign indicates which phonon eigenmodes are more important to stabilize the corresponding PM phase [4]. Figure 3 shows that in the $\mathcal{T}$ phase large and positive $\Delta\omega$'s mostly correspond to high-energy phonons ($\hbar\omega \geq 60$ meV), while in the $\mathcal{O}$ phase those are associated to relatively low-frequency modes ($\hbar\omega \sim 30$ meV). Consequently, magnetic disorder favors the $\mathcal{O}$ polymorph. At $T_c^{\rm the}(0)$, for instance, fluctuating spins provide a lattice free-energy difference of 0.168 meV/f.u. between $\mathcal{T}$ and $\mathcal{O}$, which is three-times larger than the one obtained when constraining AFM spin order.

SP-controlled transitions under compression, reentrant behavior

In most perovskites, hydrostatic pressure (P) favors the $\mathcal{O}$ phase over competing polymorphs [8, 10]. Hence, compression might help to reduce BCO's T_c and bring it closer to the AFM transition temperatures. To check this, we perform free-energy calculations as a function of pressure (see Methods). Our results are shown in Fig. 2(a).

Our prediction for the $\mathcal{T}$–$\mathcal{O}$ transition in the limit of low temperatures, $P_c^{\rm the}(0) = 3.25(0.15)$ GPa, is in fair agreement with the experimental value $P_c^{\rm exp}(0) = 3.60(0.25)$ GPa [8]. As regards the critical pressure and volume drop for this transition at room temperature, we compute 2.55(0.15) GPa and $\sim$ 11 %, respectively, while the experimental values are 2.50(0.25) GPa and $\sim$ 13 % [8]. Then, as shown in Fig. 2(a), the agreement is less satisfactory at intermediate pressures. Finally, by comparing Figs. 2(a) and 2(b), we ratify that SP effects are critical to reproduce the experiments.

Our phase diagram is rich in the region where structural and magnetic transitions get close. For $P \approx 2.5$ GPa [colored area in Fig. 2(a)], we predict that BCO presents three temperature-driven transformations: a high-T PM $\mathcal{O}$ phase followed, upon cooling, by a PM $\mathcal{T}$ phase, a G-type AFM $\mathcal{O}$ phase, and a C-type AFM

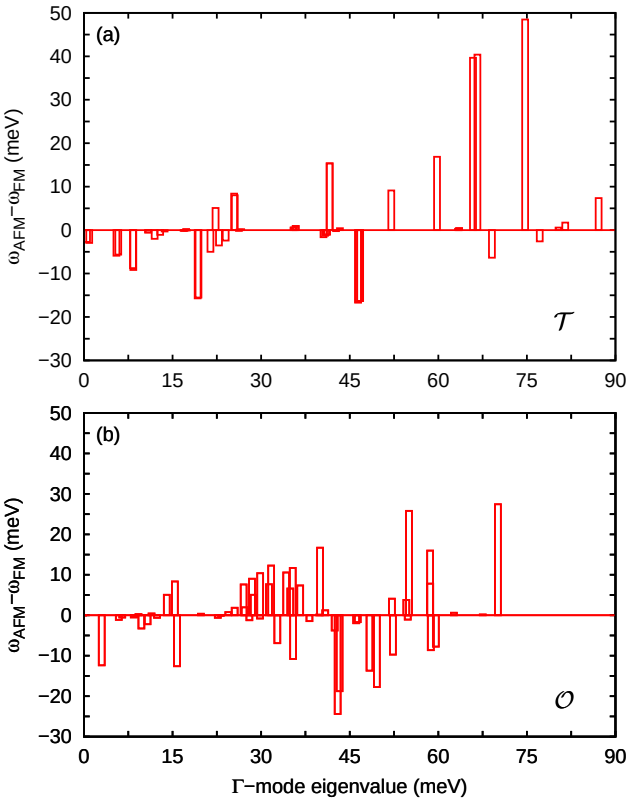

FIG. 3. Analysis of spin-phonon couplings in the $\mathcal{T}$ and $\mathcal{O}$ phases of BCO. Vibrational frequency shifts between AFM and FM spin configurations calculated at the reciprocal lattice point Γ, $\Delta\omega = \omega_{\rm AFM} - \omega_{\rm FM}$, are shown as a function of eigenmode energy (where this energy is the one obtained for the AFM ground state). Note that modes with a positive (negative) shift will tend to soften (harden) as T increases. Phonon frequency shifts for the $\mathcal{O}$ phase span over a smaller energy interval than those of the $\mathcal{T}$ phase, indicating that the former structure is vibrationally softer than the latter. In both phases, phonon eigenmodes presenting largest spin couplings correspond to medium- and high-energy excitations dominated by Co and O atoms; in contrast, low-energy eigenmodes dominated by Bi and O atoms, including those associated to the polar distortion in BCO, present small $|\Delta\omega|$ values.

$\mathcal{T}$ phase. We move from a PE to a FE phase, back to a PE structure, and finally to the FE ground state. Note that a PE-FE-PE sequence constitutes a rare reentrant behavior, as it is uncommon to stabilize a PE structure (typically more disordered) by cooling down a FE phase (typically more ordered) [11, 12]. Strikingly, here we find a double reentrance, since the low-T PE phase eventually transforms into the FE ground state.

This unprecedented PE-FE-PE-FE sequence is possible because the $\mathcal{T}$ and $\mathcal{O}$ phases display different Néel temperatures and SP couplings. In Fig. 4(a) we show the temperature dependence of the quasi-harmonic Gibbs free energy, $\tilde{G}_{\rm harm}(T)$, of BCO's polymorphs calculated at 2.5 GPa. We find that, whenever a phase becomes PM, the slope of the corresponding $\tilde{G}_{\rm harm}(T)$ curve changes noticeably; this results in three energy crossings (structural transitions) within an interval of about 325 K. The Gibbs free energy can be split in entropic [$\tilde{F}_{\rm harm}$, Fig. 4(b)] and enthalpic [$\tilde{H}_{\rm harm}$, Fig. 4(c)] terms, the latter being responsible for the slope changes accompanying the spin transitions. Such an effect, which is larger in the $\mathcal{T}$ phase, corresponds to a sizeable decrease in the thermal expansion of the crystal when spins become disordered, and is driven by SP couplings (the effect disappears for frozen spins; see Supplementary Information).

Engineering multiferroic effects at ambient conditions

The phase diagram of Fig. 2(a) suggests interesting possibilities to obtain functional properties. For example, starting from the $\mathcal{O}$-AFM phase, one could use an electric field to induce the $\mathcal{T}$ structure, which would result in either a loss of spin order (if we reach the $\mathcal{T}$-PM phase) or a transformation into a different AFM state (if we reach the $\mathcal{T}$-AFM phase with C-type order). For applications, one would like to realize such phase-change effects at ambient conditions.

Chemical substitution is a practical strategy to reduce BCO's T_c at ambient pressure. As a simple predictor for T_c, we monitor the enthalpy difference between the $\mathcal{T}$ and $\mathcal{O}$ phases at zero temperature, $\Delta H_{\rm eq}$, which is fast to compute from first principles. We thus look for chemical substitutions that yield $-0.08 \leq \Delta H_{\rm eq} \leq -0.03$ eV/f.u., to match the results for pure BCO around 2.5 GPa. We find two promising cases – namely, $BiCo_{1/2}Fe_{1/2}O_3$ and $Bi_{3/4}La_{1/4}CoO_3$ – for which the enthalpy differences (-0.075 and -0.033 eV/f.u., respectively) lie within the targeted interval. We find both compounds to be vibrationally stable; hence, they are good candidates to reproduce at ambient conditions the striking effects predicted for BCO. (See Supplementary Information for more details.)

METHODS

a. **Density Functional Theory calculations.** We use the generalised gradient approximation to density functional theory proposed by Perdew, Burke, and Ernzerhof (GGA-PBE) [13] as implemented in the VASP package [14]. We work with GGA-PBE because this is the DFT variant that provides a more accurate description of the relative stability between the $\mathcal{T}$ and $\mathcal{O}$ phases of BCO at zero temperature, as discussed in the Supplementary Information. A "Hubbard-U" scheme with $U = 6$ eV is employed for a better treatment of Co's $3d$ electrons [15]. We use the "projector augmented wave" method to represent the ionic cores [16], considering the following electrons as valence states: Co's $3p$, $3d$, and $4s$; Bi's $5d$, $6s$, and $6p$; and O's $2s$ and $2p$. Wave functions are represented in a plane-wave basis truncated at 500 eV. We use a 20-atom simulation cell that can be viewed as a $2 \times \sqrt{2} \times \sqrt{2}$ repetition of the elemental 5-

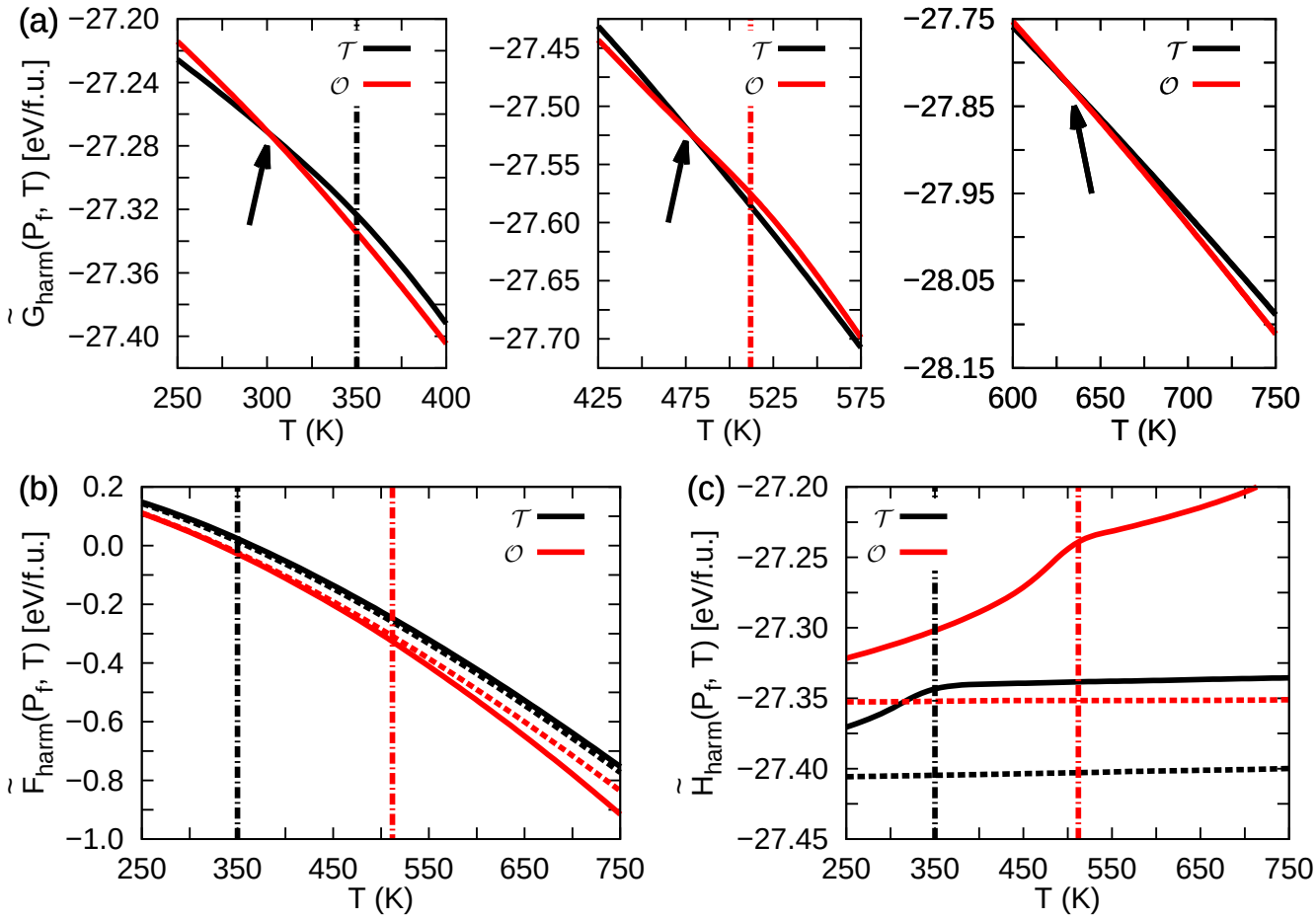

FIG. 4. Calculated quasi-harmonic free energies of BCO's competing polymorphs, as a function of temperature and at a fixed pressure $P_f = 2.5$ GPa. (a) Quasi-harmonic Gibbs free energy, $\tilde{G}_{\rm harm} \equiv \tilde{F}_{\rm harm} + \tilde{H}_{\rm harm}$; our estimates are accurate to within 5 meV per formula unit (f.u.). (b) Quasi-harmonic Helmholtz free energy, $\tilde{F}_{\rm harm} \equiv -T\tilde{S}_{\rm harm}$, where $\tilde{S}_{\rm harm}$ represents the vibrational lattice entropy. (c) Quasi-harmonic enthalpy, $\tilde{H}_{\rm harm} \equiv \tilde{E}_0 + PV$, where $P \equiv -\partial(\tilde{E}_0 + \tilde{F}_{\rm harm})/\partial V$. Black arrows indicate the occurrence of structural transitions characterized by the thermodynamic condition $\tilde{G}^{\mathcal{T}}_{\rm harm}(P_f, T_c) = \tilde{G}^{\mathcal{O}}_{\rm harm}(P_f, T_c)$. Black and red vertical lines signal magnetic spin-order transformations occurring in the $\mathcal{T}$ and $\mathcal{O}$ phases, respectively. Black and red dashed lines in (b) and (c) represent results obtained by constraining AFM magnetic spin order in our quasi-harmonic free-energy calculations, showing [panel (b)] how spin disorder tends to stabilize the $\mathcal{O}$ phase. Note that the temperature dependence of $\tilde{F}_{\rm harm}$ [panel (b)] is smooth; in contrast, the slope changes in $\tilde{H}_{\rm harm}$ [panel (c)], which are associated to the spin ordering transitions, are the main cause of the successive structural transformations.

atom perovskite unit, and which is compatible with all the crystal structures of interest here. For integrations within the Brillouin zone (BZ), we employe Γ-centered q-point grids of $6 \times 6 \times 6$. Using these parameters we obtaine enthalpy energies converged to within 0.5 meV per formula unit. Geometry relaxations are performed using a conjugate-gradient algorithm that keeps the volume of the unit cell fixed while permitting variations of its shape and atomic positions. The relaxation stops when residual forces fall below 0.01 eV·Å^{-1}. Equilibrium volumes are subsequently determined by fitting the sets of calculated energy points to Birch-Murnaghan equations of state [17]. To treat the chemical substitutions, we work with 40-atom cell that can be viewed as a 2×2×2 repetition of the elmental perovskite cell.

b. **Phonon spectrum calculations.** The calculation of phonon frequencies is performed with the direct method [18, 19], in which the force-constant matrix is calculated in real-space by considering the proportionality between atomic displacements and forces when the former are sufficiently small. Large supercells need to be constructed in order to guarantee that the elements of the force-constant matrix have all fallen off to negligible values at their boundaries, a condition that follows from the use of periodic boundary conditions [20]. Once the force-constant matrix is calculated one can Fourier-transform it to obtain the phonon spectrum at any q-point. The impact of long-range interactions on the calculation of long-wavelength phonons is disregarded as we are primarily interested in the computation of quasi-harmonic

free-energies, and in such a context this factor is known to be secondary [4]. The quantities with respect to which our phonon calculations need to be converged are the size of the supercell, the size of the atomic displacements, and the numerical accuracy in the sampling of the Brillouin zone. We find the following settings to provide quasi-harmonic free energies converged to within 5 meV per formula unit: 160-atom supercells that can be viewed as a $2 \times 2 \times 2$ multiple of the 20-atom unit mentioned above, atomic displacements of 0.02 Å, and q-point grids of $12 \times 12 \times 12$. The value of the phonon frequencies and quasi-harmonic free energies are obtained with the PHON code developed by Alfè [20]. In using this code we exploit the translational invariance of the system to impose the three acoustic branches to be exactly zero at the Γ q-point, and use central differences in the atomic forces (i.e., positive and negative atomic displacements were considered).

c. **Heisenberg model Monte Carlo simulations.** To simulate the effects of thermal excitations on the magnetic order of the $\mathcal{T}$ and $\mathcal{O}$ phases, we construct several spin Heisenberg models of the form $\hat{H} = \frac{1}{2}\sum_{ij} J_{ij}^{(0)} S_i S_j$, in which the value of the involved exchange constants is obtained from zero-temperature DFT calculations (see next section and Supplementary Information). We use such models to perform Monte Carlo (MC) simulations in a periodically-repeated simulation box of $20 \times 20 \times 20$ spins; thermal averages are computed from runs of $50,000$ MC sweeps after equilibration. These simulations allow us to monitor the T-dependence of the magnetic order through the computation of the AFM(C) (i.e., in the $\mathcal{T}$ phase) and AFM(G) (i.e., in the $\mathcal{O}$ phase) order parameters, namely, $S^{\rm C} \equiv \frac{1}{N}\sum_i (-1)^{n_{ix}+n_{iy}} S_{iz}$ and $S^{\rm G} \equiv \frac{1}{N}\sum_i (-1)^{n_{ix}+n_{iy}+n_{iz}} S_{iz}$. Here, n_{ix}, n_{iy}, and n_{iz} are the three integers locating the i-th lattice cell, and N is the total number of spins in the simulation box. For the calculation of $S^{\rm C}$ and $S^{\rm G}$, we considered only the z component of the spins because a small symmetry-breaking magnetic anisotropy was introduced in the Hamiltonian to facilitate the analysis (see Supplementary Information in Ref. [21]).

d. **Spin-phonon quasi-harmonic free-energy formalism.** We employ the approach described in Ref. [4] and generalize it to the $\mathcal{T}$ phase along the guidelines described in Ref. [21]. In this spin-phonon free-energy framework, the internal energy of the crystal is expressed as:

$$\tilde{E}_{\rm harm}(V,T) = \tilde{E}_0(V,T) + \frac{1}{2}\sum_{mn} \tilde{\Xi}_{mn}(V,T) u_m u_n \ , \quad (1)$$

where $\tilde{E}_0$ represents an effective static energy, $\tilde{\Xi}_{mn}$ an effective force constant matrix, u's atomic displacements, and the $V-T$ dependences of the various terms are explicitly noted. The Helmoltz free energy associated to the lattice vibrations, $\tilde{F}_{\rm harm} \equiv -T\tilde{S}_{\rm harm}$, is calculated by finding the eigenfrequencies of the dynamical matrix associated to $\tilde{\Xi}_{mn}$, namely, $\tilde{\omega}_{\mathbf{q}s}$, and plugging them into the formula:

$$\tilde{F}_{\rm harm}(V,T) = \frac{1}{N_q}\, k_B T \times \sum_{\mathbf{q}s} \ln\left[2\sinh\left(\frac{\hbar\tilde{\omega}_{\mathbf{q}s}(V,T)}{2k_{\rm B}T}\right)\right] \ , \quad (2)$$

where N_q is the total number of wave vectors used for integration in the Brillouin zone. Finally, the Gibbs free energy of each phase is estimated as $\tilde{G}_{\rm harm} = \tilde{E}_0 + PV + \tilde{F}_{\rm harm}$, and the hydrostatic pressure as $P = -\partial(\tilde{E}_0 + \tilde{F}_{\rm harm})/\partial V$. Our Gibbs free energy results are accurate to within 5 meV per formula unit. Transition points are determined via the condition $\tilde{G}^{\mathcal{T}}_{\rm harm}(P_c,T_c) = \tilde{G}^{\mathcal{O}}_{\rm harm}(P_c,T_c)$.

For the $\mathcal{O}$ phase, we showed in Ref. [4] that the quantities entering Eq. (1) can be calculated as:

$$\tilde{E}_0^{\mathcal{O}}(V,T) = E_0(V) + 3\gamma_a(V,T)|S|^2 J_a^{(0)} \ , \quad (3)$$

$$\tilde{\Xi}^{\mathcal{O}}_{mn}(V,T) = \Phi^0_{mn}(V) + 6\gamma_a(V,T)|S|^2 J^{(2)}_{a,mn} \ , \quad (4)$$

where $\gamma_a(V,T) \equiv \langle S_i S_j\rangle/|S|^2$ represents the correlation function between neighboring spins and $\langle ...\rangle$ the thermal average as obtained from our MC simulations. The rest of parameters in $\tilde{E}_0^{\mathcal{O}}$ and $\tilde{\Xi}^{\mathcal{O}}_{mn}$ correspond to:

$$E^0 = \frac{1}{2}\left(E^{\rm FM}_{\rm eq} + E^{\rm G}_{\rm eq}\right) \ , \quad (5)$$

$$\Phi^0_{mn} = \frac{1}{2}\left(\Phi^{\rm FM}_{mn} + \Phi^{\rm G}_{mn}\right) \ , \quad (6)$$

$$J_a^{(0)} = \frac{1}{6|S|^2}\left(E^{\rm FM}_{\rm eq} - E^{\rm G}_{\rm eq}\right) \ , \quad (7)$$

$$J^{(2)}_{a,mn} = \frac{1}{6|S|^2}\left(\Phi^{\rm FM}_{mn} - \Phi^{\rm G}_{mn}\right) \ . \quad (8)$$

In the equations above, superscripts "FM" and "G" indicate perfect ferromagnetic and antiferromagnetic G-type spin arrangements, respectively. The $J_a^{(0)}$ parameter describes the magnetic interactions when the atoms remain frozen at their equilibrium positions (see Fig. 1b); typically, this captures the bulk of the exchange couplings. Meanwhile, the $J^{(2)}_{a,mn}$ parameter captures the dependence of the phonon spectrum on the spin configuration (i.e., spin-phonon coupling effects).

For the $\mathcal{T}$ phase, we express the corresponding static energy and force constant matrix as:

$$\tilde{E}_0^{\mathcal{T}}(V,T) = E_0(V) + 2\gamma_a(V,T)|S|^2 J_a^{(0)} + \gamma_c(V,T)|S|^2 J_c^{(0)} + 4\gamma_{ac}(V,T)|S|^2 J_{ac}^{(0)} \ , \quad (9)$$

$$\tilde{\Xi}^{\mathcal{T}}_{mn}(V,T) = \Phi^0_{mn}(V) + 4\gamma_a(V,T)|S|^2 J^{(2)}_{a,mn} + 2\gamma_c(V,T)|S|^2 J^{(2)}_{c,mn} + 8\gamma_{ac}(V,T)|S|^2 J^{(2)}_{ac,mn} \ , \quad (10)$$

where $\gamma_\alpha(V,T) \equiv \langle S_i S_j\rangle/|S|^2$, with $\alpha = a, b, ac$, represent the correlation functions between in-plane and out-of-plane neighboring spins according to the sketch shown in Fig. 1(c); the rest of parameters in $\tilde{E}_0^{\mathcal{T}}$ and $\tilde{\Xi}^{\mathcal{T}}_{mn}$ can

be obtained as:

$$E^0 = \frac{1}{4}\left(E^{\rm FM}_{\rm eq} + E^{\rm A}_{\rm eq} + E^{\rm C}_{\rm eq} + E^{\rm G}_{\rm eq}\right) , \quad (11)$$

$$\Phi^0_{mn} = \frac{1}{4}\left(\Phi^{\rm FM}_{mn} + \Phi^{\rm A}_{mn} + \Phi^{\rm C}_{mn} + \Phi^{\rm G}_{mn}\right) , \quad (12)$$

$$J^{(0)}_a = \frac{1}{8|S|^2}\left(E^{\rm FM}_{\rm eq} + E^{\rm A}_{\rm eq} - E^{\rm C}_{\rm eq} - E^{\rm G}_{\rm eq}\right) , \quad (13)$$

$$J^{(2)}_{a,mn} = \frac{1}{8|S|^2}\left(\Phi^{\rm FM}_{mn} + \Phi^{\rm A}_{mn} - \Phi^{\rm C}_{mn} - \Phi^{\rm G}_{mn}\right) , \quad (14)$$

$$J^{(0)}_c = \frac{1}{4|S|^2}\left(E^{\rm FM}_{\rm eq} - E^{\rm A}_{\rm eq} + E^{\rm C}_{\rm eq} - E^{\rm G}_{\rm eq}\right) , \quad (15)$$

$$J^{(2)}_{c,mn} = \frac{1}{4|S|^2}\left(\Phi^{\rm FM}_{mn} - \Phi^{\rm A}_{mn} + \Phi^{\rm C}_{mn} - \Phi^{\rm G}_{mn}\right) , \quad (16)$$

$$J^{(0)}_{ac} = \frac{1}{16|S|^2}\left(E^{\rm FM}_{\rm eq} - E^{\rm A}_{\rm eq} - E^{\rm C}_{\rm eq} + E^{\rm G}_{\rm eq}\right) , \quad (17)$$

$$J^{(2)}_{ac,mn} = \frac{1}{16|S|^2}\left(\Phi^{\rm FM}_{mn} - \Phi^{\rm A}_{mn} - \Phi^{\rm C}_{mn} + \Phi^{\rm G}_{mn}\right) . \quad (18)$$

In the equations above, superscripts "FM", "G", "A", and "C" indicate perfect ferromagnetic, antiferromagnetic G-type, antiferromagnetic A-type, and antiferromagnetic C-type spin arrangements, respectively.

[1] Hickel, T., Grabowski, B., Körmann, F. & Neugebauer, J. Advancing density functional theory to finite temperatures: methods and applications in steel design. *J. Phys. Condens. Matter* **24**, 053202 (2012).

[2] Fang, C. M., Sluiter, M. H. F., van Huis, M. A., Ande, C. K. & Zandbergen, H. W. Origin of predominance of cementite among iron carbides in steel at elevated temperature. *Phys. Rev. Lett.* **105**, 055503 (2010).

[3] Khomskii, D. Classifying multiferroics: Mechanisms and effects. *Physics* **2**, 20 (2009).

[4] Cazorla, C. & Íñiguez, J. Insights into the phase diagram of bismuth ferrite from quasiharmonic free-energy calculations. *Phys. Rev. B* **88**, 214430 (2013).

[5] Glazer, A. M. The classification of tilted octahedra in perovskites. *Acta Crystallographica Section B* **28**, 3384 (1972).

[6] Arnold, D. C., Knight, K. S., Morrison, F. D. & Lightfoot, P. Ferroelectric-paraelectric transition in $BiFeO_3$: crystal structure of the orthorhombic β phase. *Phys. Rev. Lett.* **102**, 027602 (2009).

[7] Belik, A. A., Iikubo, S., Kodama, K., Igawa, N., Shamoto, S., Niitaka, S., Azuma, M., Shimakawa, Y., Takano, M., Izumi, F. & Takayama-Muromachi, E. Neutron powder diffraction study on the crystal and magnetic structures of $BiCoO_3$. *Chem. Mater.* **18**, 798-803 (2006).

[8] Oka, K., Azuma, M., Chen, W.-T., Yusa, H., Belik, A. A., Takayama-Muromachi, E., Mizumaki, M., Ishimatsu, N., Hiraoka, N., Tsujimoto, M., Tucker, M. G., Attfield, J. P. & Shimakawa, Y. Pressure-induced spin-state transition in $BiCoO_3$. *J. Am. Chem. Soc.* **132**, 9438 (2010).

[9] Hong, J., Stroppa, A., Íñiguez, J., Picozzi, S. & Vanderbilt, D. Spin-phonon coupling effects in transition-metal perovskites: a DFT+U and hybrid-functional study. *Phys. Rev. B* **85**, 054417 (2012).

[10] Guennou, M., Bouvier, P., Chen, C. S., Dkhil, B., Haumont, R., Garbarino, G. & Kreisel, J. Multiple high-pressure phase transitions in $BiFeO_3$. *Phys. Rev. B* **84**, 174107 (2011).

[11] Pociecha, D. *et al.* Reentrant ferroelectricity in liquid crystals. *Phys. Rev. Lett.* **86**, 3048 (2001).

[12] Aydinol, M.K., Mantese, J.V., Alpay, S.P. A comparative ab initio study of the ferroelectric behaviour in KNO_3 and $CaCO_3$. *J. Phys.: Condens. Matt.* **19**, 496210 (2007).

[13] Perdew, J. P., Burke, K. & Ernzerhof, M. Generalized gradient approximation made simple. *Phys. Rev. Lett.* **77**, 3865 (1996).

[14] Kresse, G. & Fürthmuller, J. Efficient iterative schemes for ab initio total-energy calculations using a plane-wave basis set. *Phys. Rev. B* **54**, 11169 (1996); Kresse, G. & Joubert, D. From ultrasoft pseudopotentials to the projector augmented-wave method. *Phys. Rev. B* **59**, 1758 (1999).

[15] Diéguez, O. & Íñiguez, J. First-principles investigation of morphotropic transitions and phase-change functional responses in $BiFeO_3$-$BiCoO_3$ multiferroic solid solutions. *Phys. Rev. Lett.* **107**, 057601 (2011).

[16] Blöchl P. E. Projector augmented-wave method. *Phys. Rev. B* **50**, 17953 (1994).

[17] Cazorla, C. & Boronat, J. First-principles modeling of three-body interactions in highly compressed solid helium. *Phys. Rev. B* **92**, 224113 (2015).

[18] Kresse, G., Furthmüller, J. & Hafner, J. Ab initio force constant approach to phonon dispersion relations of diamond and graphite. *Europhys. Lett.* **32**, 729 (1995).

[19] Alfè, D., Price, G. D. & Gillan, M. J. Thermodynamics of hexagonal-close-packed iron under Earths core conditions. *Phys. Rev B* **64**, 045123 (2001).

[20] Alfè, D. PHON: a program to calculate phonons using the small displacement method. *Comp. Phys. Commun.* **180**, 2622 (2009).

[21] Escorihuela-Sayalero, C., Diéguez, O. & Íñiguez, J. Strain engineering magnetic frustration in perovskite oxide thin films. *Phys. Rev.Lett.* **109**, 247202 (2012).

ACKNOWLEDGMENTS

This research was supported under the Australian Research Council's Future Fellowship funding scheme (project number FT140100135), the Israel Science Foundation through Grants 1814/14 and 2143/14, and the Luxembourg National Research Fund through the PEARL (Grant P12/4853155 COFERMAT) and CORE (Grant C15/MS/10458889 NEWALLS) programs. Computational resources and technical assistance were provided by RES and the Australian Government through Magnus under the National Computational Merit Allocation Scheme.

AUTHOR CONTRIBUTIONS

All authors contributed equally to the present work.

ADDITIONAL INFORMATION

Supplementary information accompanies this paper at xxx.

Competing financial interests: The authors declare no competing financial interests.